AGU PUBLICATIONS

Geochemistry, Geophysics, Geosystems

RESEARCH ARTICLE
10.1002/2014GC005445

The relationship between seismicity and fault structure on the Discovery transform fault, East Pacific Rise

Monica Wolfson-Schwehr[1], Margaret S. Boettcher[1], Jeffrey J. McGuire[2], and John A. Collins[2]

[1]Department of Earth Sciences, University of New Hampshire, Durham, New Hampshire, USA, [2]Department of Geology and Geophysics, Woods Hole Oceanographic Institution, Woods Hole, Massachusetts, USA

Key Points:
- Rupture patches and rupture barriers observed on Discovery transform fault
- Step-overs in the fault trace >1 km are not required to terminate ruptures
- Rate of microseismicity varies between rupture patches and rupture barriers

Supporting Information:
- Supporting Information Text01

Correspondence to:
M. Wolfson-Schwehr,
monica.schwehr@gmail.com

Citation:
Wolfson-Schwehr, M., M. S. Boettcher, J. J. McGuire, and J. A. Collins (2014), The relationship between seismicity and fault structure on the Discovery transform fault, East Pacific Rise, *Geochem. Geophys. Geosyst.*, *15*, 3698–3712, doi:10.1002/2014GC005445.

Received 9 JUN 2014
Accepted 16 AUG 2014
Accepted article online 21 AUG 2014
Published online 29 SEP 2014

Abstract There is a global seismic moment deficit on mid-ocean ridge transform faults, and the largest earthquakes on these faults do not rupture the full fault area. We explore the influence of physical fault structure, including step-overs in the fault trace, on the seismic behavior of the Discovery transform fault, 4S on the East Pacific Rise. One year of microseismicity recorded during a 2008 ocean bottom seismograph deployment (24,377 $0 \leq M_L \leq 4.6$ earthquakes) and 24 years of Mw $\geq$ 5.4 earthquakes obtained from the Global Centroid Moment Tensor catalog, are correlated with surface fault structure delineated from high-resolution multibeam bathymetry. Each of the 15 $5.4 \leq$ Mw ≤ 6.0 earthquakes that occurred on Discovery between 1 January 1990 and 1 April 2014 was relocated into one of five distinct rupture patches using a teleseismic surface wave cross-correlation technique. Microseismicity was relocated using the HypoDD relocation algorithm. The western fault segment of Discovery (DW) is composed of three zones of varying structure and seismic behavior: a zone with no large events and abundant microseismicity, a fully coupled zone with large earthquakes, and a complex zone with multiple fault strands and abundant seismicity. In general, microseismicity is reduced within the patches defined by the large, repeating earthquakes. While the extent of the large rupture patches on DW correlates with physical features in the bathymetry, step-overs in the primary fault trace are not observed at patch boundaries, suggesting along-strike heterogeneity in fault zone properties controls the size and location of the large events.

1. Introduction

The Discovery transform fault, located at 4S on the East Pacific Rise (EPR, Figure 1), is ideal for investigating the relationship between seismic processes and fault structure. Discovery is a segmented transform fault, comprising two fault strands separated by an intratransform spreading center. Both fault strands contain multiple repeating-rupture patches that host Mw 5.4–6.0 earthquakes [*McGuire*, 2008]. Discovery was the site of a 2008 ocean bottom seismometer (OBS) deployment, as well as two high-resolution multibeam bathymetry surveys in 2006 and 2008. The bathymetry data enable the surface structure of the fault trace of Discovery to be delineated on a subkilometer scale, while the OBS data provide a high-resolution seismic database. These two data sets, combined with a 24 year record of seismicity obtained from the global Centroid Moment Tensor (CMT) catalog [*Dziewoński et al.*, 1981; *Ekström et al.*, 2012], are used to investigate whether fault structure influences seismic behavior along the segmented Discovery transform fault.

Discovery is representative of a typical mid-ocean ridge transform fault (RTF) in that the size and repeat time of the largest observed earthquakes scale with the seismogenic area of the fault [*Boettcher and Jordan*, 2004; *Boettcher and McGuire*, 2009]. The largest observed earthquakes on Discovery (Mw 6.0) are small compared to the full fault area and repeatedly rupture the same patch of the fault (Figure 2) [*McGuire*, 2008; *Boettcher and McGuire*, 2009]. Multiple large rupture patches occur on each fault segment and these patches fail when an accumulation of ~50–100 cm of tectonic slip has been reached since the last large event, corresponding to a mean repeat time of 5.8 years [*McGuire*, 2008]. While the majority of plate motion on RTFs is accommodated aseismically [*Bird et al.*, 2002; *Boettcher and Jordan*, 2004], the largest events on many intermediate and fast-slipping RTFs occur on fully coupled fault patches [*Braunmiller and Nábělek*, 2008; *McGuire*, 2008; *Boettcher and McGuire*, 2009; *Sykes and Ekström*, 2012] separated by rupture barriers with low seismic coupling [*McGuire*, 2008; *McGuire et al.*, 2012].

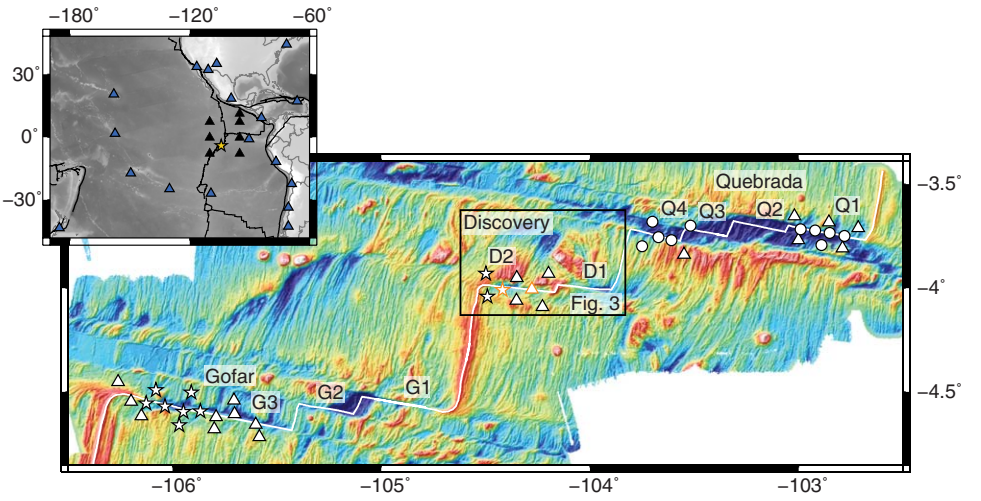

Figure 1. Base map: 2006 SeaBeam 2112 bathymetry data of the Quebrada, Discovery, and Gofar transform faults. Fault segments are numbered following *Searle* [1983]. In the text, D1 and D2 are referred to as DE and DW for clarity. Data are gridded at a 200 m resolution. White circles, triangles, and stars, respectively, indicate the locations of the short period, broadband, and broadband plus strong motion seismometers deployed during the 2008 OBS experiment. The star and triangle bordered in orange on Discovery represent stations D01 and D07, respectively. These two stations are referenced in section 4. The rectangle surrounding the Discovery transform fault delineates the area shown in Figure 3. Inset: Smith and Sandwell global topography data (v 15.1, 2013) for the equatorial Pacific. Blue triangles indicate the location of GSN stations used in the relocation analysis. Black triangles indicate the positions of the NOAA PMEL hydroacoustic array during the 1996–2001 deployment. Discovery is indicated by the gold star.

In 2008, *McGuire et al*. [2012] positioned an OBS array consisting of 30 broadband seismometers (10 collocated with strong-motion accelerometers) and 10 short-period seismometers on the Quebrada, Discovery, and Gofar transform fault system (QDG) on the EPR for a period of approximately 1 year (Figure 1), and successfully captured an Mw 6.0 earthquake on the westernmost segment (G3) of Gofar on 18 September 2008. In the 2 weeks prior to this event, more than 20,000 foreshocks were recorded on the OBS array [*McGuire et al*., 2012]. These foreshocks clustered in a 10 km long zone located just east of the mainshock rupture patch. To the east of the foreshock zone is another rupture patch, which last failed in 2007 (Mw 6.2). Neither the 2008 nor the 2007 earthquakes appear to have ruptured across the foreshock region and into the adjacent patch. These observations indicate that there are regions of the fault that act both as barriers to large rupture propagation as well as loci for abundant microseismic activity, suggesting that the mechanical properties of the fault zone (the fault core and/or damage zone) vary along strike [*McGuire et al*., 2012].

On continental strike-slip faults, *Wesnousky* [2006] found that fault step-overs on the order of 5 km in width act as physical barriers to rupture propagation. Along RTFs, compressional or dilational step-overs, intratransform spreading centers, and pull-apart basins can divide the fault into a series of parallel or subparallel fault segments [*Searle*, 1983] that may create barriers to rupture propagation. On Gofar, there appears to be a small jog in the fault trace at the western terminus of the foreshock zone, corresponding to a compressional bend at depth as evidenced by the microseismicity [*McGuire et al*., 2012; *Froment et al.,* 2014]. The coincidence of this feature with the location of the barrier zone suggests that it may influence rupture propagation.

In this study, we examine the relationship between surface fault structure and the location and size of repeating-rupture patches, as well as the spatial relationship between rupture patches and microseismicity on the Discovery transform fault. We use two multibeam bathymetry data sets, SeaBeam 2012 data collected in 2006 (grid resolution: 200 m) and EM300 data collected in 2008 (grid resolution: 75 m), to delineate the fault trace on a subkilometer scale and relate the bathymetry to the locations of large (Mw $\geq$ 5.4) earthquakes that have occurred from 1992 to 2013 and microseismicity ($0 \leq M_L \leq 4.6$) recorded on Discovery during the 2008 OBS deployment. The goal of this study is to improve our understanding of how plate motion is accommodated along oceanic transform boundaries by investigating the influence of fault structure on the seismic behavior of the Discovery transform fault.

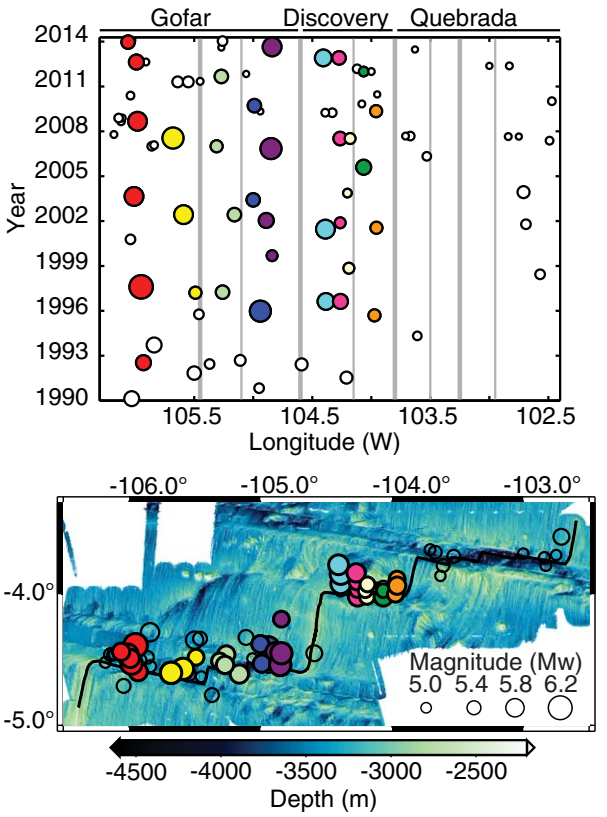

Figure 2. Map and space-time evolution of Mw $\geq$ 5.0 earthquakes on Quebrada, Discovery, and Gofar transform faults between 1 January 1990 and 1 March 2014, modified from *McGuire* [2008] and *McGuire et al.* [2012]. All earthquakes (circles) are sized by magnitude. Events on Quebrada and Gofar are shown at their CMT catalog locations. Events on Discovery are shown at their relocated longitude, and are offset in latitude so that all events are visible on the map. Earthquakes with overlapping ruptures (defined as relative centroid locations <5 km) [see *McGuire* 2008] are represented by circles of the same color. The vertical gray lines denote the location of mid-ocean ridge segments (thick lines) and intratransform spreading centers (thin lines).

2. Structure of the Discovery Transform Fault

The Discovery transform fault is a fast-slipping, left-lateral fault system composed of two subparallel fault strands separated by an intratransform spreading center [*Searle*, 1983] (ITSC; Figures 1 and 3). The slip-rate on Discovery is ~12.6 cm/yr according to the Global Strain Rate Model (GSRM v1.2) [*Kreemer et al.*, 2003]. In contrast to Gofar and Quebrada, on Discovery there is a distinct lack of fracture zones beyond the ridge-transform intersections, and Discovery's strike (~95 degrees) forms an obtuse angle with the EPR. These observations are consistent with findings from earlier studies suggesting that the plate geometry of the QDG fault system is still evolving [*Fox and Gallo*, 1989; *Forsyth et al.*, 2007; *Pickle et al.*, 2009]. The segments of Discovery are both defined by median valleys, and include dilational features (nodal basins and the ITSC) consistent with a component of extension across Discovery caused by the obtuse angle between Discovery and the EPR.

The western fault segment of Discovery (DW) is 36 km long and is defined by three distinct structural zones (Figures 3b and 3c). Zone A, the westernmost zone, is composed of a narrow and well-defined (300–500 m wide) fault valley extending from the ridge-transform intersection to 7 km along strike. Heading east, the fault valley broadens into two consecutive lozenge-shaped basins that comprise zone B. The first basin is 4 km long, 2 km wide, and ~600 m deep relative to the surrounding seafloor. A small, 0.75 km wide ridge separates this basin from the larger, 7.5 km long, 2.5 km wide basin to the east (Figure 3b, purple arrow). Here the strike of the fault trace changes from approximately east-west to more west-northwest to east-southeast. This larger basin is the deepest part of DW, ~900 m below the surrounding seafloor, and is terminated at its eastern extent by a 3.5 km wide ridge that crosscuts the transform valley (Figures 3b and 3c, yellow arrow). Zone C, the third structural zone, begins east of this ridge, where there is a series of 3–5 km long en echelon ridges (Figure 3b, pink arrow), which may be small fault strands making up a splay zone. This series of ridges is bounded to the south by the primary fault trace, and to the north by a 17 km long secondary fault trace.

The eastern fault segment of Discovery (DE) is composed of a single 27 km long fault zone that progressively widens from a narrow, well-defined fault trace at the ITSC into a broad, 4.5 km wide nodal basin along the inside corner of the eastern ridge-transform intersection (Figures 3b and 3c). The deepest part of DE occurs within the nodal basin and is ~1150 m below the surrounding seafloor (Figure 3c). Small changes in strike (< 15°) occur along DE; the most notable of which are found where the fault zone begins to widen ~8 km east of the ITSC and where it enters the nodal basin ~15 km east of the ITSC.

The bathymetric expression of the ITSC separating the two segments of Discovery is broad and flat, with an average base width of 6 km and an average crest width of 1.4 km (Figure 3). The offset distance between

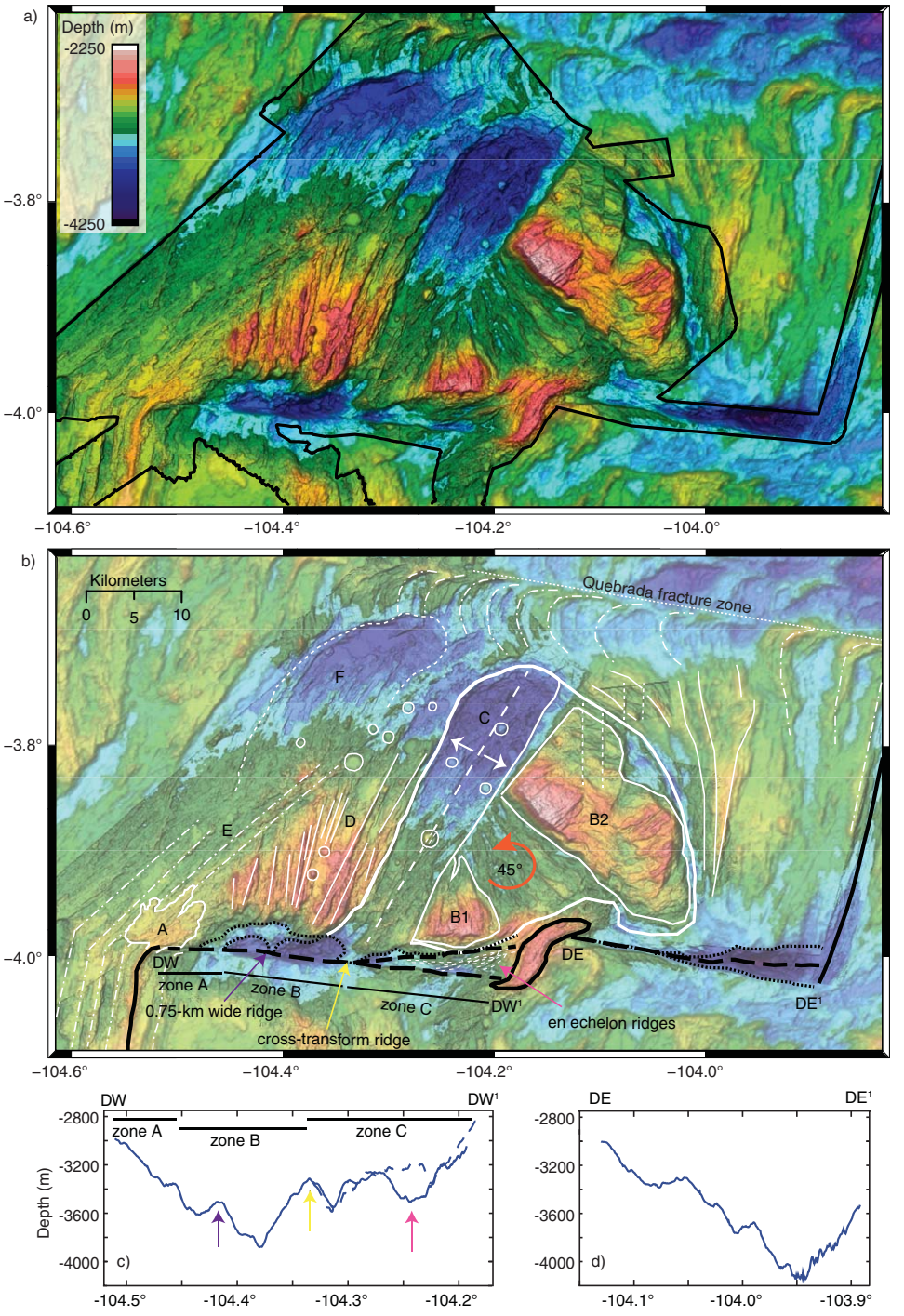

Figure 3. (a) Bathymetry of the Discovery transform fault and possible nanoplate. Foreground data: 75 m resolution EM300 multibeam bathymetry data collected in 2008. Background data: 200 m resolution SeaBeam 2112 multibeam bathymetry data collected in 2006. Both data sets use the same color scale. (b) Interpreted geology of the Discovery transform fault and possible nanoplate. A: axis-centered ridge-transform intersection high; B1 & B2: rotated crustal blocks; C: rift; D: north-south ridges; E: NE-SW trending abyssal hills; and F: abandoned rift. The thick white line outlines the region of rotated terrain that comprises the possible nanoplate. Solid white lines denote apparent compressional ridges. Long-dashed white lines indicate extensional zones and arrows indicate direction of extension. Short-dashed white lines indicate possible faults that offset features. White dashed-dotted lines highlight abyssal hill fabric. Circles outline some of the seamounts in the area. Black solid lines show the location of the EPR on either end of Discovery and outline the intratransform spreading center. Black long-dashed lines show the primary fault traces; short-dashed black line indicates the secondary trace on the western segment. Black-dotted lines outline the two consecutive lozenge-shaped valleys on the western fault segment, and delineate the width of the fault valley. Orange arrow denotes direction of rotation of the nanoplate. (c) Cross section with depth from DW to DW^1 of the western fault segment. (d) Cross section with depth from DE to DE^1 of the eastern fault segment.

the primary fault traces of DW and DE is ~8 km; however, the total length of the ITSC is 14 km. The excess length results from sigmoidal shape of the ITSC, which may be due to fissure eruptions creating volcanic ridges extending at acute angles to the spreading direction, similar to the Joseph Mayes seamount on the Southwest Indian Ridge [*Dick et al*., 2003]. Discovery's ITSC comprises a region of thickened crust [*Pickle et al*., 2009], reaching a height of 700 m above the surrounding seafloor. It is anomalous compared to the ITSCs of Quebrada and Gofar, which are defined by axial valleys, such as those generally associated with slow-spreading ridges. *Pickle et al*. [2009] used gravity data along with the Seabeam 2112 bathymetry data set to infer crustal thickness throughout the QDG region. They found that the ITSCs on Quebrada and Gofar are well-established spreading centers, defined by a thin crust, variable melt supply, and depressed thermal structure. Conversely, the ITSC on Discovery recently developed as the fault changed configuration, and may represent a region of constructive volcanism over a preexisting plate.

The 70 km long ridge segment of the EPR linking Discovery with Gofar to the south is relatively narrow (1.5–5 km) and has a shallow axial high consistent with observations from many fast-spreading ridges, e.g., *Small* [1998] and *Shah and Buck* [2001] (Figure 3). The intersection between this ridge segment and DW (feature A, Figure 3b) is characterized by an "axis-centered" intersection high [*Barth et al*., 1994]. Similar morphology has been observed at the RTIs of other transform faults on the EPR, including Clipperton [*Gallo et al*., 1986; *Barth et al*., 1994], Quebrada [*Lonsdale*, 1978], and Raitt [*Lonsdale*, 1994], and is thought to result from some combination of lateral heat transport across the fracture zone leading to thermal expansion [*Gallo et al*., 1986; *Phipps Morgan and Forsyth*, 1988], and constructive/intrusive volcanism due to excess ridge volcanism [*Gallo et al*., 1986; *Kastens et al*., 1986].

The 35 km long EPR segment connecting Discovery with Quebrada to the north is characterized by a 5 km wide spreading center and a 200–300 m deep axial valley (Figure 3). Given the fast spreading rates associated with the EPR, the presence of a median valley along this ridge segment is unexpected. *Pickle et al*. [2009] attributes this to the possibility that a portion of the extension between the Pacific and Nazca plates along this ridge segment may be accommodated by the formation of grabens and dike injections to the west, effectively reducing the spreading rate along the ridge [*Forsyth et al*., 2007].

Directly north of the ITSC on Discovery, there is an ~850 km^2 region of complex, discordant terrain (Figure 3). Rotated crustal blocks containing oblique abyssal hill fabric (features B1 and B2, Figure 3b) are present within this region, and suggest a counterclockwise rotation of ~45 degrees [*Forsyth et al*., 2007]. This region is bounded to the west (104.3W) by a 7 km wide rift, or pull-apart basin (feature C, Figure 3b), that extends 35 km northeast of Discovery. A set of ridges (feature D, Figure 3b) that trend roughly north-south and bound the rift to the west is truncated to the northwest by abyssal hill fabric (feature E, Figure 3b) that cuts across the ridges at an angle of ~45 degrees. The rift progressively deepens and curves slightly inward toward the northeast at its northern extent. Stair-stepped morphology along the flanks of seamounts (white circles in Figure 3b) within the rift indicates normal faulting. The morphology of the rift, specifically the deepening and inward curvature of the tip, is strikingly similar to the secondary rifts bounding the Wilkes nanoplate [*Goff et al*., 1993] located at 9S on the EPR, the Easter Island microplate [*Naar and Hey*, 1991] located at 25S on the EPR, and the Juan Fernandez micro plate [*Bird et al*., 1998] located at 33S on the EPR. An apparent abandoned rift segment (feature F, Figure 3b) located northwest of the rift, overprints the oblique abyssal hill fabric west of this region, suggesting that the abyssal hills predate the rotation and formation of this complex region. Small ridges and troughs bound this region to the north and east. Similar ridges and troughs are observed at the Wilkes nanoplate, where the free-air gravity anomaly suggests these features are formed, in part, by compressional upwarping and downwarping of the crust [*Goff et al*., 1993]. The similarity between the morphology of the deformed region just north of Discovery and that at the Wilkes nanoplate suggests a similar mechanism of formation.

3. Repeating-Rupture Patches

To determine the role fault structure plays in controlling the location and size of rupture patches on Discovery, it was first necessary to determine absolute locations for the large repeating earthquakes because location errors of up to ~50 km are common for mid-ocean earthquakes in global seismic catalogs [*Sverdrup*, 1987; *Cronin and Sverdrup*, 2003]. Following the relative surface-wave relocation technique described in *McGuire* [2008], earthquakes detected by the National Oceanic and Atmospheric Administration (NOAA)

hydroacoustic catalog were used as empirical Greens Functions (EGFs) to determine the absolute location for an Mw 5.5 earthquake in 1998. This event was subsequently used to estimate the absolute centroid locations of all other Mw $\geq$ 5.4 events that occurred between 1992 and 2013 using relative surface-wave arrival times.

The hydroacoustic earthquake catalog is compiled by NOAA's Pacific Marine Environmental Laboratory (PMEL) using data from a suite of hydrophone arrays, which were deployed in the eastern equatorial Pacific between 19 May 1996 and 19 October 2002 (Figure 1). The hydrophones record the tertiary waves (T-wave or T-phase) of earthquakes, i.e., the seismic energy of an earthquake that leaves the seafloor and travels through the water column as an acoustic wave. While uncertainties associated with T-phase source locations are small inside the hydroacoustic array ($<$ 2 km) [*Fox et al*., 2001], this location does not necessarily represent the true epicenter or centroid of the earthquake, but rather the point at which most of the seismic energy leaves the oceanic crust and is converted into acoustic energy. To avoid location bias that may be introduced by topographic steering [*Fox et al*., 2001; *Smith*, 2003], only events located on or near the fault trace, away from topographic highs were used in this analysis.

Thirteen events located by the hydroacoustic catalog were used to relocate the 1998 Mw 5.5 earthquake that ruptured a fault patch centrally located on Discovery, just west of the ITSC. Events from the hydroacoustic catalog were chosen on the basis of their magnitude (Mw $\geq$ 4.4) and location (events $>$ 5 km off the fault trace or located on a topographic high were excluded). Each of these earthquakes was used as an EGF to compute a relative location for the 1998 Mw 5.5 event using a cross correlation of the first orbital Rayleigh (R1) waves. The nucleation depth for earthquakes on RTFs is thought to be constrained by the 600°C isotherm [*Abercrombie and Ekström*, 2001; *Boettcher et al*., 2007], which is relatively shallow for fast-slipping transforms on the EPR ($\leq$ 6 km). The relative depth and distance between each EGF and the 1998 Mw 5.5 event ($<$ 25 km) is small compared to the teleseismic distance between the events and the Global Seismic Network (GSN) stations ($>$ 1000s km); therefore, path effects between the EGF and the master event are assumed negligible. Seismicity in the NOAA hydroacoustic catalog is predominantly associated with transform faults, indicating that the focal mechanisms for these events should correspond to strike-slip motion on near-vertical faults [*Fox et al*., 2001]. Given the similarity in location and focal mechanism, the R1 arrivals from the EGF and the target event are expected to have similar waveforms at the GSN stations. The primary differences between the two waveforms at a specific station are phase and amplitude, corresponding to differential arrival time and relative seismic moment, respectively [*McGuire*, 2008].

For each event, seismograms were obtained from a set of GSN stations that are azimuthally distributed around Discovery (Figure 1). The data were bandpass filtered between 0.02 and 0.04 Hz to isolate the R1 arrivals, as this bandwidth has a high signal-to-noise ratio and constant group velocity (3.7 km/s) for R1 waves in young oceanic lithosphere [*Nishimura and Forsyth*, 1988]. Waveform pairs with a cross-correlation coefficient $\geq$ 0.7 were used to compute the relative distance between events. The differential times were measured from the peak of the cross-correlation function and obvious outliers ($>$3 standard deviations from the mean) were removed. The remaining differential times were then fit to a cosine function using the L1 norm to minimize the effect of any outliers that fell below the 3 standard deviation cutoff. The scale and phase parameters of the cosine fit were used to obtain a relative distance and azimuth between the EGF and the master event (Figure 4). As in *McGuire* [2008], standard errors were computed for the parameters of the cosine fit using a bootstrap algorithm and assuming a Gaussian distribution with a 1 s standard deviation for the differential travel-time measurement errors. The errors were calculated as the standard deviation in location estimates after 100 iterations. Each event pair resulted in a single estimated location for the 1998 Mw 5.5 earthquake; these estimations were averaged to obtain the best estimate of the absolute centroid position (Table 1 and Figure 5a). Three of the 13 event pairs resulted in either a poor cosine fit, or a location estimate that was more than 5 km off the fault, and their estimated locations were not included in the average.

Three of the 10 events from the hydroacoustic catalog that were used in the relocation of the 1998 Mw 5.5 earthquake were also recorded in the CMT catalog. To ensure no circularity was introduced into our location procedure, we compared the location of the 1998 event obtained from averaging all 10 estimated locations with that obtained from averaging only estimated locations based on the seven events unique to the hydroacoustic catalog. The location estimate based on the seven events is $\sim$0.5 km east of the location estimate based on all 10 earthquakes. The estimated absolute location of an event becomes more precise as

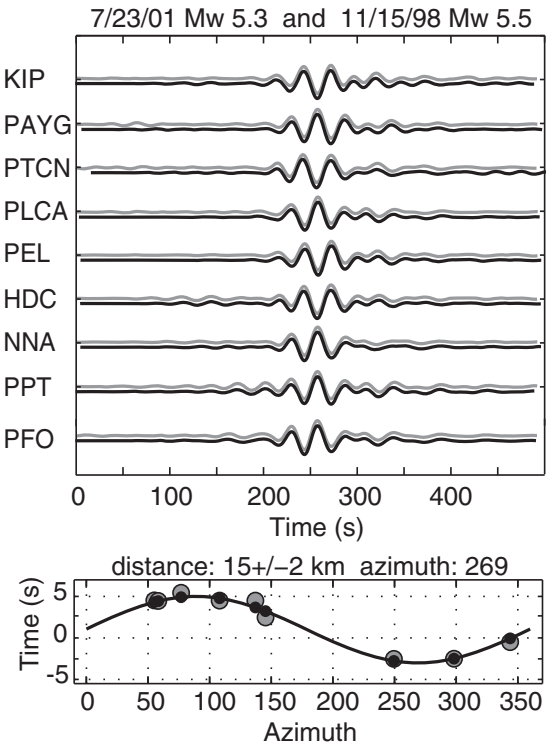

Figure 4. Relative relocation of the 1998 Mw 5.5 master event using a 2001 Mw 5.3 event located by the NOAA/PMEL hydroacoustic catalog as an EGF. (a) Aligned Rayleigh waves of the EGF (gray) and master event (black) filtered between 0.02 and 0.04 Hz at GSN stations. (b) Differential arrival times (gray) and best fit estimates from the cosine function (black). The master event is located 15 km from the NOAA/PMEL event, at an azimuth of 269 degrees.

the number of relative position estimates averaged together increases (uncertainty reduces by a factor of $1/\sqrt{N}$). A discrepancy of 0.5 km is within the reduced uncertainty of our averaged location (~0.6 km), and is therefore not significant.

The 1998 Mw 5.5 event was then used as an EGF to estimate the absolute positions for the remaining 14 Mw $\geq$ 5.4 earthquakes on Discovery recorded in the CMT catalog between 1992 and 2013 (Table 2 and Figure 5b). Each relocated event fell into one of five distinct patches; three on the DW (patches DW1, DW2, DW3) and two on DE (patches DE1, DE2) (Figure 6). These rupture patches, defined as areas on the fault where overlapping ruptures (centroids $\leq$ 5 km apart) repeatedly occur, include the four patches initially identified by *McGuire* [2008] and one additional patch with earthquakes in 2005 and 2012 (dark green circles in Figure 2). There was an Mw 5.6 earthquake in 1991 that may have ruptured either DW2 or DW3, but there were too few reliable stations to compute a robust location.

Mean rupture lengths were estimated for each rupture patch using:

$$R_L = \left(\frac{M_{0avg}}{\Delta\sigma}\right)^{2/3} Z^{-1} \quad (1)$$

where M_{0avg} is the averaged seismic moment release of all earthquakes belonging to that patch, $\Delta\sigma$ is the static stress drop that is assumed to be constant at 3 MPa [*Allmann and Shearer*, 2009; *Boettcher and McGuire*, 2009], and Z is the maximum depth of rupture that is assumed to be 5 km, consistent with the mean depth of the microseismicity on Discovery and Gofar [*McGuire et al*., 2012]. To obtain equation (1), we follow *Boettcher and Jordan* [2004] and assume average earthquake slip, D, scales as the square root of the rupture area, A, as $D=\Delta\sigma\mu^{-1}A^{1/2}$. Combining the equation for D with the equation for seismic moment $M_0=\mu AD$, where μ, the shear modulus, is 44.1 GPa, the value obtained for the lower crust from the Preliminary Earth Reference Model (PREM) [*Dziewonski and Anderson*, 1981] gives us equation (1).

Table 1. Hydroacoustic (t-Phase) Events Used in the Relocation of the 1998 Mw 5.5 Event[a]

Event #	Latitude	Longitude	Date	Time	Mw	Estimated 1998 Event Latitude	Estimated 1998 Event Longitude
1	−3.9970	−104.3990	23 Aug 1996	21:56:16	5.9	−4.0269	−104.2096
2	−4.0070	−104.2530	23 Aug 1996	22:19:06	5.9	−4.0353	−104.1658
3	−4.0120	−104.0020	8 Jun 1997	21:02:43	5.1	−4.0253	−104.1933
4	−4.0180	−103.9090	12 Aug 1997	3:49:49	4.4	−4.0090	−104.1674
5	−4.0360	−103.9580	7 May 2000	6:18:45	4.4	−4.0281	−104.1830
6	−4.0170	−104.2200	26 Jun 2001	15:22:32	4.7	−4.0331	−104.1908
7	−4.0150	−103.9870	23 Jul 2001	10:34:34	5.1	−4.0050	−104.1785
8	−3.9810	−104.0680	23 Jul 2001	9:43:08	5.3	−3.9833	−104.2014
9	−3.9930	−104.0400	23 Jul 2001	10:06:57	4.4	−3.9875	−104.1983
10	−4.0290	−103.9760	23 Jul 2001	4:34:49	5.6	−4.0168	−104.2092
Averaged centroid location for the 1998 Mw 5.5 event:						−4.0150	−104.1897

[a]Dates and times are UTC.

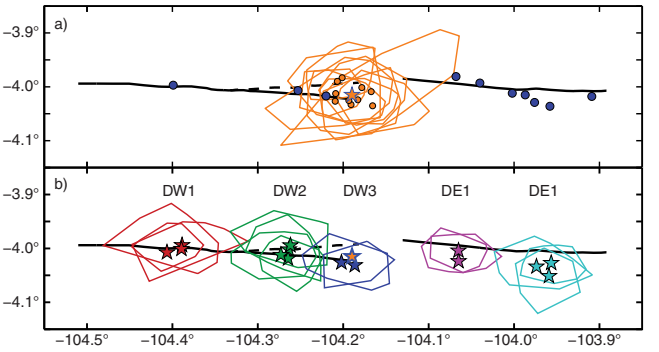

Figure 5. (a) Relocation of the 1998 Mw 5.5 earthquake. Blue circles show the location of events from the NOAA/PMEL hydroacoustic catalog used to calculate relative positions for the 1998 event. Orange circles denote relative position estimates of the 1998 event. The orange polygons outline the uncertainty in each relative position estimated from the bootstrap algorithm described in the text. The orange star with the blue border represents the absolute centroid of the 1998 event obtained by averaging the relative relocations. (b) Relocation of the repeating Mw $\geq$ 5.4 earthquakes in the CMT catalog. Stars represent the estimated centroid positions relative to the 1998 Mw 5.5 event. Polygons outline the estimated uncertainty in position. In both plots, the black lines denote the western and eastern fault traces of the Discovery transform (solid: primary, dashed: secondary).

Rupture patch DW1 has an estimated length of 10 km and is the largest patch on Discovery, hosting Mw 5.9–6.0 earthquakes (Figure 6). Rupture patch DW2 is located ~5 km east of patch DW1 and hosts Mw 5.5–5.8 earthquakes with an estimated rupture length of ~6 km. The smallest rupture patch on Discovery is DW3, located just west of the ITSC. DW3 has a length of ~3 km and fails in Mw 5.4–5.5 events.

The calculated locations for the two 5 km long rupture patches on DE (patches DE1 and DE2) are just south of the fault trace (Figure 6). Patch DE1 is located 9 km east of the ITSC and is ~2 km south of the transform valley. Patch DE2, the easternmost rupture patch, is located ~3 km south of the fault valley. This is likely due to event mislocation. Figure 5b shows the location uncertainty associated with each earthquake relocated in this study, calculated using the bootstrap method. For both patches, the fault trace is within the computed location uncertainty. There is additional uncertainty associated with the velocity structure underlying Discovery. The relocation scheme assumes an R1 wave velocity value that is representative of young oceanic lithosphere and does not take into account localized variations. While the path effects between the EGF and the event being relocated is typically considered negligible compared to the path effects between the events and the GSN stations, it is possible that there is some unknown local variation, particularly underlying the ITSC, that is significant enough to affect the relocation scheme. These uncertainties, combined with the lack of fault structure south of the eastern segment in the bathymetry data suggest that patch DE1 and DE2 actually lie on the eastern fault trace.

4. Microseismicity

The 2008 OBS deployment on the QDG fault system recorded 24,377 earthquakes ($0.16 \leq M_L \leq 4.58$, magnitude of completeness for DW: 0.9 and DE: 2.0) on Discovery between 1 January and 31 December. There were no large repeating earthquakes on Discovery during the deployment period. The Antelope software package was used to generate an earthquake catalog from the OBS data using standard short-term average to long-term average (STA/LTA)-based detection algorithms [*Houliston et al.*, 1984] for P-waves and wavelet-based detections [*Simons et al.*, 2006] for S-wave arrivals (see supporting information for detailed methodology). On DW, the majority of earthquakes in the catalog cluster within 5 km of the primary fault trace (gray circles, Figure 7). Earthquakes extend outside both the western RTI (Figure 7; Area I) and eastern ITSC-intersection (Figure 7; Area II). There is a 2 km long zone located at

Table 2. Estimated Centroid Locations of the 15 Mw $\geq$ 5.4 Repeating Earthquakes[a]

Rupture Patch	Date	Time	Latitude	Longitude	Mw
DW1	23 Aug 1996	21:56:13	−4.0010	−104.3893	5.9
	26 Jun 2001	12:34:00	−3.9941	−104.3887	6.0
	17 Dec 2012	17:41:37	−4.0740	−104.4068	5.9
DW2	23 Aug 1996	22:19:04	−3.9944	−104.2616	5.8
	29 Nov 2001	17:07:06	−4.0020	−104.2634	5.5
	23 Jul 2007	6:03:55	−4.0189	−104.2644	5.6
	17 Dec 2012	17:46:50	−4.0121	−104.2726	5.8
DW3	15 Nov 1998	4:51:49	−4.0150	−104.1897	5.5
	26 Nov 2003	17:32:55	−4.0267	−104.2022	5.4
	23 Jul 2007	6:00:38	−4.0318	−104.1867	5.5
DE1	21 Aug 2005	9:49:54	−4.0237	−104.0647	5.8
	17 Jan 2012	15:27:52	−4.0041	−104.0649	5.4
DE2	16 Sep 1995	22:49:22	−4.0339	−103.9733	5.6
	30 Jul 2001	4:34:50	−4.0272	−103.9565	5.6
	24 May 2009	9:57:16	−4.0514	−103.9591	5.7

[a]Dates and times are UTC.

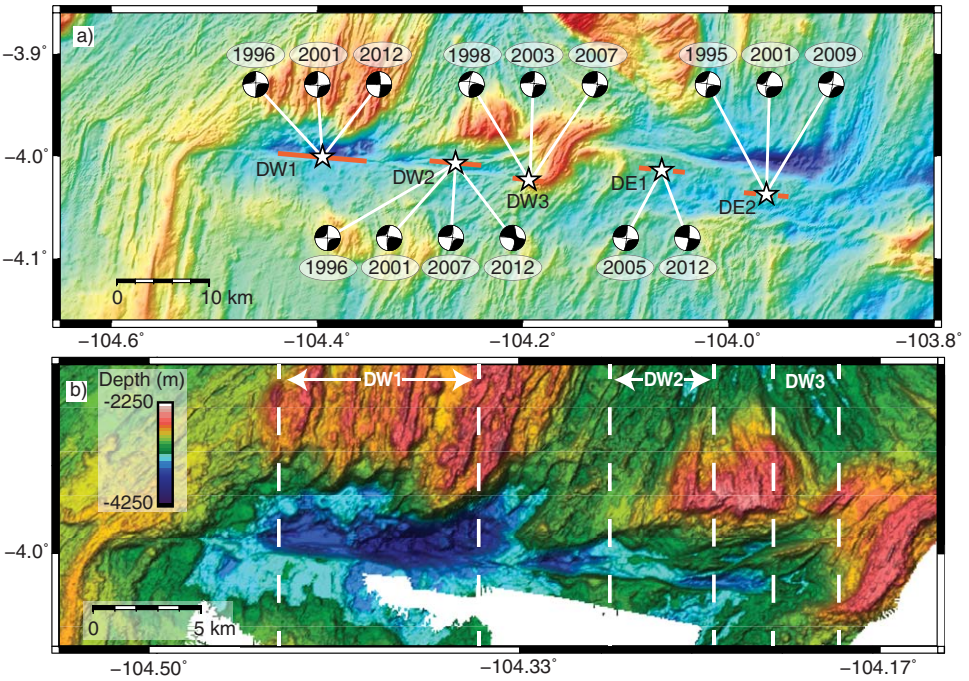

Figure 6. (a) Repeating-rupture patch locations on the Discovery transform fault. White stars denote the averaged location of earthquake centroids for each patch. Red lines represent the estimated rupture length centered on each centroid. The repeating earthquakes in each rupture patch are shown by their focal mechanism and year. (b) A zoomed in view of the fault structure and extent of the rupture patches on DW.

∼104.5W on the western fault segment in which very few earthquakes occurred (Figure 7; Area III). A small cluster of earthquakes is located on the crustal block just north of the possible splay zone (∼104.22W). On DE, which is outside the OBS array, the majority of recorded earthquakes cluster north of the transform valley within 16 km of the ITSC.

Earthquakes in the Antelope-generated catalog were relocated using the HypoDD double-difference algorithm [*Waldhauser and Ellsworth*, 2000] to estimate more robust positions. The microseismicity was divided into seven overlapping groups, subset by longitude (Figure 7). Groups 1–4 cover DW, group 5 is centered on the ITSC, and groups 6 and 7 cover DE. The earthquakes within group 7 were located > 20 km outside of the OBS array and were not relocatable. Only earthquakes that had detections on five or more stations (minimum of 10 associated P and S arrivals) were used in the relocation analysis (17,017 events). Differential

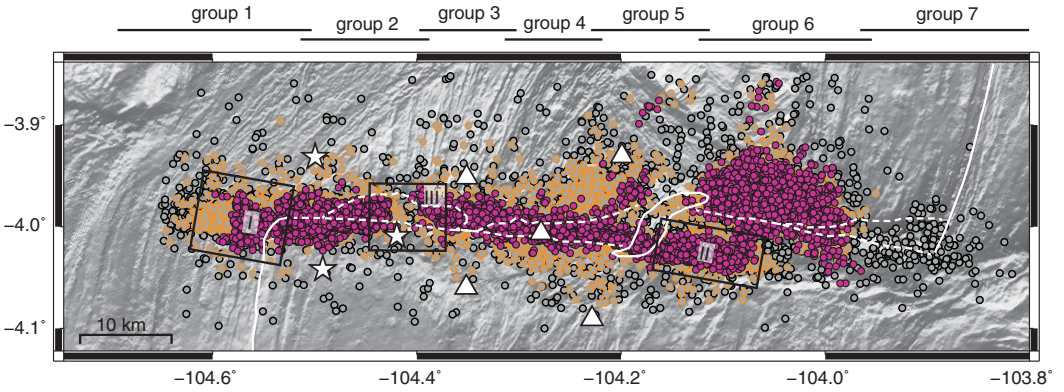

Figure 7. Microseismicity on the Discovery transform fault. Gray circles: STA/LTA catalog locations. Gray circles with orange border: events from the STA/LTA catalog that were successfully relocated by HypoDD. Pink circles: relocated positions. White solid lines denote the location of the EPR and outline the ITSC. White-dashed lines indicate the width of the fault valley on both the western and eastern fault segments. Areas I, II, and III are described in the text.

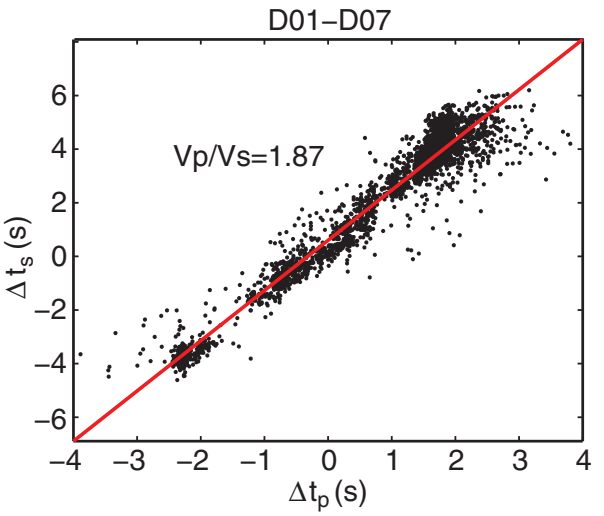

Figure 8. The difference in S-wave first arrival times (*y* axis) versus P-wave (*x* axis) first arrival times for microearthquakes on DW recorded at stations D01 and D07 (see Figure 1 for station locations). The red line represents a linear least squares regression to the data and is indicative of the Vp/Vs ratio in the lower crust between the two stations.

arrival times were calculated via waveform cross correlation for P and S waves. A window of 2.56 s centered on the arrival was extracted from each waveform, and subsequently tapered and bandpass filtered between 5–12 Hz for S waves and 5–15 Hz for P waves. Event pairs required a minimum of six differential time observations per pair with a cross-correlation coefficient ≥ 0.75. Catalog arrival times were not used due to the higher uncertainty associated with the increased percentage of misidentified phases. The relocation of events within groups 1–4 were based on a minimum of nine observations per event pair, as these groups fall within, or directly adjacent to, the OBS array. Relocations for events within groups 5 and 6 were based on a minimum of eight and six observations per pair, respectively, as these groups are located increasingly farther outside the OBS array. A one-dimensional version of the P-wave velocity model developed by *Roland et al*. [2012] for the Gofar transform fault was used. The Vp/Vs ratio of 1.87 was obtained by fitting a linear least squares regression to differential S-wave versus P-wave arrival times for the two stations located on the fault trace (D01 and D07; Figures 1 and 8). This Vp/Vs ratio is on the upper end of the expected range from studies of oceanic crustal rocks [*Christensen*, 1972; *Anderson*, 1989; *Barclay et al*., 2001] and may reflect localized high porosity, as was interpreted by *Roland et al*. [2012] and *McGuire et al*. [2012] for Gofar.

A total of 12,635 earthquakes out of the original 17,017 (∼74%) were successfully relocated using the HypoDD algorithm (pink circles in Figure 7). For events located inside the overlapping region of two groups, final location estimates were obtained by averaging the relocated positions (median difference in position estimates from all overlapping groups is ∼1.8 km). The large cluster of events on DE tightens up slightly, but remains predominantly located north of the fault trace. These events fall outside the OBS array, thus their locations are less certain than those on DW. Along DW, the location of the microseismicity tightened up along the fault trace so that 95% of events were within 3 km of the fault trace. The latitudinal spread of the microseismicity is likely due to a combination of unaccounted for location uncertainty and the occurrence of events in the damage zone surrounding the fault core [e.g., *Valoroso et al*., 2014]. Microseismic activity extends ∼4.5 km outside the western RTI and ∼9 km beyond the ITSC intersection. The region of reduced seismicity in Area III is more distinct in the relocated catalog. Earthquakes on either side of this region have moved outward relative to their initial locations, forming a gap within which there is no microseismicity at all.

Perhaps the most striking observation is the extension of microseismic activity beyond the western RTI and ITSC intersection (Areas I and II; Figure 7); such activity is not observed on the neighboring Gofar transform fault. Although seismic activity has been observed along the fracture zones of other RTFs, these events are primarily associated with shorter-lived aftershock sequences related to mainshocks that occurred on the active transform [*Bohnenstiehl et al*., 2004] or complex stress regimes related to the Mendocino Triple Junction [*Sverdrup*, 1987]. On Discovery, the extension of microseismicity beyond the active fault boundaries occurs throughout the entire deployment period. Comparison of waveform arrivals between a few of the events located west of the RTI and events located on the active western fault segment suggest that these events do occur outside the RTI and are not mislocated (see supporting information). The extension of events beyond the endpoints of DW is in line with the general trend of seismicity on the active fault trace and with the strike of the fault itself, suggesting that events in Areas I and II (Figure 7) may be related to the propagation of fracture zones. The change in the strike of the microseismicity from approximately east-west to more northwest-southeast coincides with the change in strike of the active fault trace, and indicates that

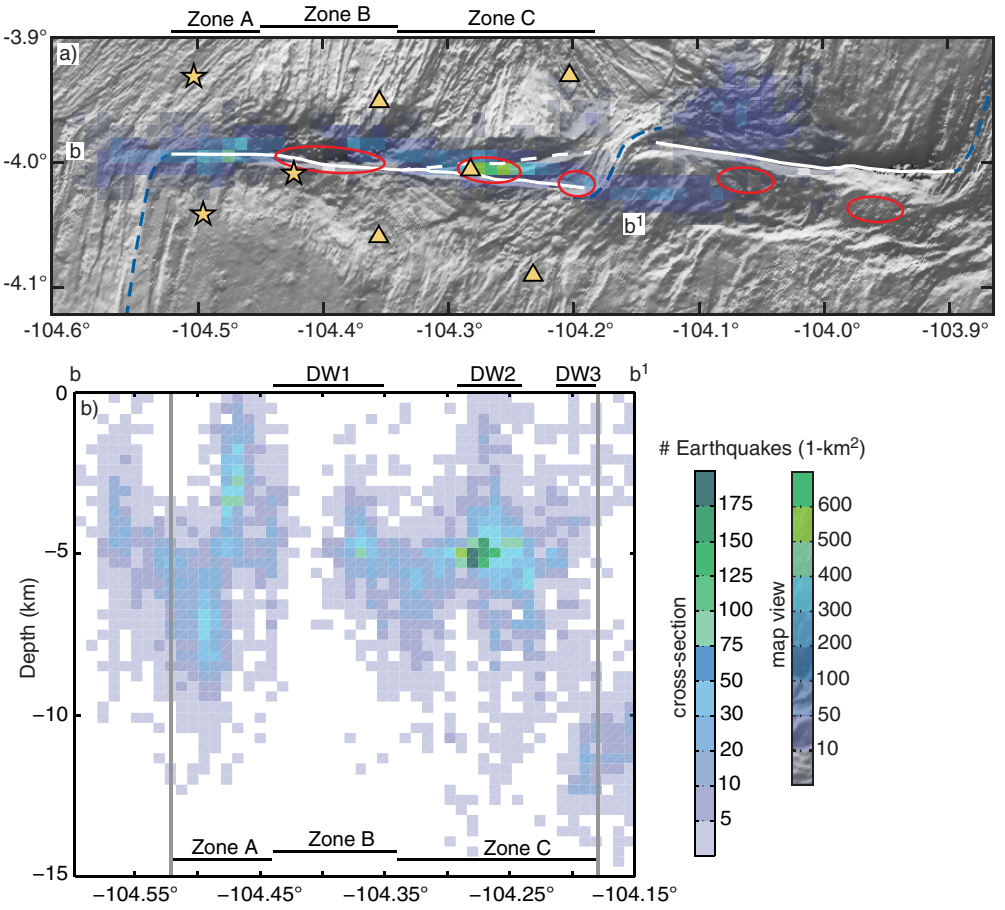

Figure 9. (a) Map view of the seismicity on the Discovery transform fault. Red ellipses are centered on the rupture patch centroid locations and indicate rupture length. Microseismicity is represented as a density plot (boxes are 1 km-by-1 km). White lines denote the primary (solid) and secondary (dashed) fault trace. Blue-dashed lines denote the ridge segments and the ITSC. Gold stars represent the broadband seismometers and gold triangles indicate broadband seismometers with strong motion sensors. The density plot shows that the majority of recorded microseismicity occurs along the western fault segment. The highest density coincides with rupture patch 2, located in the splay zone. The seismic gap coincides with DW1, the largest rupture patch. (b) Cross section along the western segment of Discovery showing a density plot of the microseismicity with depth for b–b^1. All microseismicity is projected into a single vertical plane. Boxes are 1 km-by-1 km. Vertical gray lines indicate the location of the EPR and ITSC.

the surface fault trace reflects aspects of the fault structure at depth. The inflection point in the strike of the microseismicity appears to lie within the 3 km long microseismic gap (Area III; Figure 7). This gap appears to be real (see supporting information), reflecting an area of the fault that was completely locked during the OBS deployment. *McGuire and Collins* [2013] used seafloor geodesy to show that within millimeter-level precision, this part of the fault was indeed locked during 2008.

5. Discussion

The relationship between seismicity and fault structure in zones A and B on DW (Figure 9) is strikingly similar to what is observed on the western end of the G3 segment of the Gofar transform fault, also studied during this experiment (Figures 1 and 2) [*McGuire et al*., 2012; *Froment, et al.,* 2014] where strongly coupled fault patches are separated by zones of abundant microseismicity that do not appear to rupture in the large earthquakes. Zone A on Discovery comprises the narrow, well-defined fault trace that extends from the RTI eastward ~7 km along the fault. This zone appears to be a barrier to large ruptures as there are no Mw > 5 earthquakes recorded in this region over the 45 year span of the CMT catalog (see Figure 2 for the past 24 years), although the CMT catalog is only complete down to Mw 5.4 for QDG. Zone A is structurally and mechanically comparable to western end of G3 [*McGuire et al*., 2012; *Froment et al*., 2014], which is also relatively narrow, well-defined, devoid of large events, and contains abundant microseismicity. On both faults,

the western RTI is defined by an intersection high that spills over onto the older plate with prominent abyssal hill fabric. Microseismicity on westernmost G3 appears to split into two branches, suggesting that the fault zone in this region may be composed of two subparallel fault strands [*Froment, et al.,* 2014].

Zone B encompasses the largest repeating-rupture patch on Discovery, DW1, which is located in the deepest portion of the fault within the two adjacent lozenge-shaped valleys. The gap in the microseismicity is located within zone B, coinciding with the centroid location of patch DW1 (Figure 9). The lack of microseismicity in the large rupture patch is consistent with the accumulation of a slip deficit between earthquakes and supports the interpretations that the patch is fully coupled. The extent of rupture patch DW1 corresponds to the narrowing and shallowing of the transform valley as it exits the two consecutive valleys at either end of zone B. The eastern extent of DW1 also coincides with the 3.5 km wide cross-transform ridge (Figure 3b, yellow arrow). Mechanically, zone B on DW is comparable to segment 2 on G3, which includes the rupture patch that hosted the 2008 Mw 6.0 earthquake [*Froment, et al.,* 2014]. Microseismicity within the Mw 6.0 rupture patches on G3 during the interseismic period is minimal [*McGuire et al*., 2012], similar to DW1.

The clear pattern observed on both western G3 and western DW, where a large rupture patch is confined by small-scale bathymetric features and surrounded by zones of low seismic coupling and high rates of microseismicity, is not observed in zone C on DW. Zone C is the most complex region of Discovery. The highest density of microseismicity, two repeating-rupture patches, DW2 and DW3, and a zone of small en echelon ridges that extend from the cross-transform ridge to the ITSC are all located within zone C (Figure 9). The high concentration of microseismicity within zone C coincides with the location of DW2, suggesting very different behavior to that observed for DW1 and the G3 rupture patches. It is possible that the secondary fault trace and some of the small en echelon fault strands are active in addition to the primary fault trace, and may accommodate some of the microseismicity in this zone. There is a small cluster of earthquakes between patches DW2 and DW3. Patch DW3 contains some microseismicity, though some of this seismicity may be associated with activity on the ITSC.

The majority of the microseismicity on DW locates in the crust shallower than 6 km (Figure 9b), as expected from the short transform fault length and fast slip rate on Discovery, consistent with observations on Gofar [*McGuire et al*., 2012]. While some microseismicity in Figure 9b appears to extend well into the upper mantle, these depths are not well constrained due to insufficient station spacing. The depth resolution is poorest outside of the array, where the deepest seismicity is shown.

On both G3 and DW, small structural features on the order of 0.5-km or greater coincide with some of the rupture patch boundaries. On G3, there appears to be an ~600 m wide step-over in the fault trace at the western end of the foreshock zone that separates the two large repeating-rupture patches. This step-over coincides with a 600 m long bend in the trend of the microseismicity as it exits the foreshock zone [*Froment et al*., 2014]. On DW, the structural features that correlate with the extents of the rupture patches do not appear to offset the primary fault trace in the cross-transform direction, though the ability to detect such offsets is limited by the resolution of the bathymetry data (75–200 m).

Observations from both Discovery and Gofar suggest that step-overs in the fault trace are not required for a structural feature to act as a barrier to rupture propagation. Small structural features, including step-overs in the fault trace, may be associated with an increased damage zone width or intensity. Enhanced fracturing in the damage zone may allow for increased porosity and subsequent dilatant strengthening during large events, providing a mechanism for halting rupture propagation. Increased porosity has been invoked to explain the observed decrease in P-wave velocities in the foreshock zone on G3 in the weeks leading up to the Mw 6.0 mainshock [*McGuire et al*., 2012; *Roland et al*., 2012]. Dilatant step-overs in the fault trace have been observed to stop rupture on continental strike-slip faults [*Sibson*, 1987; *Harris and Day*, 1993; *Wesnousky*, 2006], through a process thought to involve extensional fracturing at the rupture tip, leading to reduction in fluid pressure and subsequent dilatant strengthening [*Sibson*, 1987]. Compressional step-overs may also stop rupture due to an increase in the mean and normal stresses acting on the fault [*Harris and Day*, 1993; *Wesnousky*, 2006]. In both cases, field observations on continental strike-slip faults [*Knuepfer*, 1989; *Wesnousky*, 2006] agree with dynamic rupture models [*Harris and Day*, 1993] and indicate a step-over of ~5 km will stop rupture propagation. Furthermore, *Harris and Day* [1993] found that in dynamic rupture models, the dimension of fault step required to stop rupture was dependent on rupture velocity and stress

drop. For subshear rupture-velocities and stress drops of 3 MPa, compressional and dilational step-overs were found to stop rupture at dimensions less than 1 km.

Even with the complexity in zone C, all but one of the structural features in the fault trace that we are able to resolve (Figure 3) correlate with either the boundary of a large earthquake rupture patch or are the foci of abundant microseismicity (Figure 9). Rupture patch DW2 is bounded to the west by the narrowing of the possible splay zone as it approaches the cross-transform ridge. The eastern terminus of DW2 may be associated with one of the en echelon faults that make up the possible splay zone. Patch DW3 is the smallest rupture patch on Discovery and is located just west of the ITSC. The eastern end of DW3 extends to the ITSC-intersection. The length scale of segmentation derived from the structural complexity in zone C matches the length of rupture patches DW2 and DW3. The only feature that is not observed to correlate with either the end of a repeating-rupture patch or abundant microseismicity is the small, 0.75 km wide ridge that separates the two lozenge-shaped valleys located near the center of the DW1 rupture patch in zone B.

The relationship between fault structure and seismicity on the eastern segment of Discovery is not well constrained. DE is composed of a single fault valley that progressively widens from a narrow, well-defined fault trace near the ITSC to a broad, deep nodal basin approaching the eastern RTI. DE hosts two repeating-rupture patches, DE1 and DE2, as well as a cluster of microseismicity located just north of the fault trace (Figure 9). The OBS network did not cover DE, which significantly increased the magnitude of completeness and reduced the location accuracy of the recorded microseismicity. In addition, the 1998 Mw 5.5 event used to relocate the large, repeating earthquakes was located on DW. It is possible that the velocity structure under the ITSC may have influenced the relocation procedure, and thus reduced the accuracy of the large events locations on DE compared with DW. Acknowledging the uncertainty in the large event locations, it appears that DE1 occurs along the part of the fault that is still relatively narrow and well defined, while DE2 is located within the nodal basin.

Evidence of stress-transfer can be seen in three sets of Mw $\geq$ 5.4 earthquakes that occur minutes apart in adjacent patches. On 23 August 1996, DW2 hosted a Mw 5.8 earthquake $\sim$23 min after a Mw 5.9 earthquake ruptured DW1. The same pattern repeated on 17 December 2012, with only $\sim$6 min between events. On 23 July 2007, DW3 ruptured in a Mw 5.5 earthquake $\sim$3 min prior to a Mw 5.6 rupture on patch DW2. In all three cases, the second earthquake was located about 1–2 rupture lengths from the first, and patch DW2 was the last to rupture. These observations suggest that either static or dynamic stress transfer may be an important triggering mechanism on DW.

Liu et al. [2012] modeled seismic cycles on RTFs using rate and state-dependent friction to explore the relationship between earthquake behavior and global RTF scaling relations. This model does not require along-fault heterogeneity in material properties in order to satisfy the observed scaling relations of *Boettcher and Jordan* [2004] and *Boettcher and McGuire* [2009], but it does require large nucleation zone sizes and an increase in the characteristic slip distance with fault width. The results of *Liu et al*. [2012] correspond to a multimode hypothesis of earthquake rupture [*Boettcher and Jordan*, 2004] in which a fault patch transitions between seismic and aseismic slip over many earthquake cycles. In these models, the large earthquakes jump around between cycles nucleating in different patches of the fault until eventually the entire fault has ruptured. The Mw $\geq$ 5.4 earthquakes observed on Discovery and Gofar, however, repeatedly rupture the same fault patches over the 24 years of the CMT catalog used in this study (Figure 2), following the single-mode hypothesis of *Boettcher and Jordan* [2004] and suggesting that rupture patches and barriers remain stable over multiple seismic cycles. Therefore, along-strike heterogeneity in fault properties is likely the cause of the slip deficit.

6. Conclusions

This study examined the correlation between fault structure and seismic behavior on the Discovery transform fault, located at 4S on the East Pacific Rise. The western fault segment of Discovery is composed of three distinct mechanical zones, including a zone that acts as a barrier to large rupture propagation, with no large earthquakes and abundant microseismicity, a fully coupled zone with large earthquakes, and a complex zone with multiple fault strands and abundant seismicity. While fracture zone traces are not evident in the bathymetry, microseismicity extends beyond the western RTI and the ITSC intersection, suggesting nascent fracture zone formation. The rotated block of complex terrain centered immediately north of

the ITSC may be an active nanoplate similar to that just north of the Wilkes transform fault, and suggests a complex regional stress regime surrounding Discovery. The obtuse angle of Discovery to the EPR combined with the lack of fracture zones and extension of microseismicity beyond the active fault trace suggest that Discovery is a relatively young and still evolving transform fault.

The primary focus of this study is whether or not structural features evident in the bathymetry data, including small step-overs in the surface fault trace, are a controlling factor in the size and location of the large, repeating-rupture patches. There are no step-overs in the fault trace $\geq$ 1 km that coincide with the endpoints of the large rupture patches on Discovery. Rupture patch boundaries do correlate with other structural features that do not offset the fault trace, such as the 3.5 km wide cross-transform ridge and the small en echelon faults, suggesting that step-overs greater than 1 km are not required to terminate ruptures on RTFs. The large repeating-rupture patches are separated by 5–10 km long regions that do not rupture in Mw $\geq$ 5.4 earthquakes. The rate of microseismicity varies strongly between the largest rupture patch (DW1) and the neighboring regions of the fault zone, similar to what is observed on Gofar. These observations suggest that along-strike heterogeneity in fault and damage zone properties partitions RTFs into regions that either fail in large, repeating earthquakes or regions that act as barriers to large rupture propagation and generate abundant microseismicity. It is these heterogeneities, rather than any large ($\geq$ 1 km wide) step over in the fault trace, that appear to limit the size of the largest repeating earthquakes on RTFs and prevent them from rupturing the whole fault.

Acknowledgments

The authors would like to acknowledge N. Hayman, L. Sykes, and D. Bohnenstiehl for reviewing the manuscript and proving critical feedback. We thank D. Smith and B. Froment for comments and feedback during the writing of this manuscript. J.V. Gardner provided valuable discussions during the bathymetric analysis. D. Forsyth and R. Pickle provided the SeaBeam 2112 data collected in 2006 aboard the R/V Knorr. We thank the crews of both the R/V Knorr and the R/V Thomas G. Thomspon for their hard work during the 2006 (KN182-13, 27 March 2006–6 May 2006) and 2008 (TN214, 15 December 2007–17 January 2008) research cruises. Multibeam bathymetry data are available online via the Marine Geoscience Data System. The OBS data used in this research was provided by instruments from the Ocean Bottom Seismograph Instrument Pool (www.obsip.org) which is funded by the National Science Foundation. OBSIP data are archived at the IRIS Data Management Center (www.iris.edu). The W. M. Keck Foundation provided financial support to build the 10 broadband seismometers that carried strong-motion accelerometers. This material is based on work supported by NSF grant OCE-024211 with additional support under grant OCE-1352565. Funding was also provided by the NOAA grant NA10NOS4000073.

References

Abercrombie, R. E., and G. Ekström (2001), Earthquake slip on oceanic transform faults, *Nature*, *410*(6824), 74–77.

Allmann, B. P., and P. M. Shearer (2009), Global variations of stress drop for moderate to large earthquakes, *J. Geophys. Res.*, *114*, B01310, doi:10.1029/2008JB005821.

Anderson, D. L. (1989), The crust and upper mantle, in *Theory of the Earth*, pp. 45–62, Blackwell Sci., Boston, Mass.

Barclay, A. H., D. R. Toomey, and S. C. Solomon (2001), Microearthquake characteristics and crustal V_P/V_S structure at the mid-Atlantic ridge, 35°N, *J. Geophys. Res.*, *106*(B2), 2017–2034, doi:10.1029/2000JB900371.

Barth, G. A., K. A. Kastens, and E. M. Klein (1994), The origin of bathymetric highs at ridge-transform intersections: A multi-disciplinary case study at the Clipperton Fracture Zone, *Mar. Geophys. Res.*, *16*(1), 1–50.

Bird, P., Y. Y. Kagan, and D. D. Jackson (2002), Plate tectonics and earthquake potential of spreading ridges and oceanic transform faults, in *Plate Boundary Zones, Geophys. Monogr. Ser.*, vol. 30, edited by S. Stein and J. T. Freymueller, pp. 203–218, AGU, Washington, D. C.

Bird, R. T., D. F. Naar, R. L. Larson, R. C. Searle, and C. R. Scotese (1998), Plate tectonic reconstructions of the Juan Fernandez microplate: Transformation from internal shear to rigid rotation, *J. Geophys. Res.*, *103*(B4), 7049–7067, doi:10.1029/97JB02133.

Boettcher, M. S., and T. H. Jordan (2004), Earthquake scaling relations for mid-ocean ridge transform faults, *J. Geophys. Res.*, *109*, B12302, doi:10.1029/2004JB003110.

Boettcher, M. S., and J. J. McGuire (2009), Scaling relations for seismic cycles on mid-ocean ridge transform faults, *Geophys. Res. Lett.*, *36*, L21301, doi:10.1029/2009GL040115.

Boettcher, M. S., G. Hirth, and B. Evans (2007), Olivine friction at the base of oceanic seismogenic zones, *J. Geophys. Res.*, *112*, B01205, doi:10.1029/2006JB004301.

Bohnenstiehl, D. R., M. Tolstoy, and E. Chapp (2004), Breaking into the plate: A 7.6 Mw fracture-zone earthquake adjacent to the Central Indian Ridge, *Geophys. Res. Lett.*, *31*, L02615, doi:10.1029/2003GL018981.

Braunmiller, J., and J. Nábělek (2008), Segmentation of the Blanco Transform Fault Zone from earthquake analysis: Complex tectonics of an oceanic transform fault, *J. Geophys. Res.*, *113*, B07108, doi:10.1029/2007JB005213.

Christensen, N. I. (1972), The abundance of serpentinites in the oceanic crust, *J. Geol.*, *80*(6), 709–719.

Cronin, V. S., and K. A. Sverdrup (2003), Multiple-event relocation of historic earthquakes along Blanco Transform Fault Zone, NE Pacific, *Geophys. Res. Lett.*, *30*(19), 2001, doi:10.1029/2003GL018086.

Dick, H. J. B., J. Lin, and H. Schouten (2003), An ultraslow-spreading class of ocean ridge, *Nature*, *426*, 405–412.

Dziewonski, A. M., and D. L. Anderson (1981), Preliminary reference Earth model, *Phys. Earth Planet. Inter.*, *25*(4), 297–356, doi:10.1016/0031–9201(81)90046-7.

Dziewoński, A. M., T. A. Chou, and J. H. Woodhouse (1981), Determination of earthquake source parameters from waveform data for studies of global and regional seismicity, *J. Geophys. Res.*, *86*(B4), 2825–2852, doi:10.1029/JB086iB04p02825.

Ekström, G., M. Nettles, and A. M. Dziewoński (2012), The global CMT project 2004–2010: Centroid-moment tensors for 13,017 earthquakes, *Phys. Earth Planet. Inter.*, *200*, 1–9, doi:10.1016/j.pepi.2012.04.002.

Forsyth, D. W., L. Kerber, and R. Pickle (2007), Co-existing overlapping-spreading-center and ridge-transform geometry, *Eos Trans. AGU*, *88*(52), Fall Meet. Suppl., Abstract T32B–05.

Fox, C. G., H. Matsumoto, and T.-K. A. Lau (2001), Monitoring Pacific Ocean seismicity from an autonomous hydrophone array, *J. Geophys. Res.*, *106*(B3), 4183–4206, doi:10.1029/2000JB900404.

Fox, P. J., and D. G. Gallo (1989), Transforms of the Eastern Pacific, in *The Eastern Pacific Ocean and Hawaii*, edited by E. L. Winterer, D. M. Hussong, and R. W. Decker, pp. 111–124, Geol. Soc. of Am., Boulder, Colo.

Froment, B., J. J. McGuire, R. D. van der Hilst, P. Gouédard, E. C. Roland, H. Zhang, and J. A. Collins (2014), Imaging along-strike variations in mechanical properties of the Gofar transform fault, East Pacific Rise, *J. Geophys. Res.*, doi:10.1002/2014JB011270, in press.

Gallo, D. G., P. J. Fox, and K. C. Macdonald (1986), A Sea Beam investigation of the Clipperton transform fault: The morphotectonic expression of a fast slipping transform boundary, *J. Geophys. Res.*, *91*(B3), 3455–3467, doi:10.1029/JB091iB03p03455.

Goff, J. A., D. J. Fornari, J. R. Cochran, C. Keeley, and A. Malinverno (1993), Wilkes transform system and "nannoplate," *Geology*, *21*(7), 623–626.

Harris, R. A., and S. M. Day (1993), Dynamics of fault interaction: Parallel strike-slip faults, *J. Geophys. Res.*, *98*(B3), 4461–4472, doi:10.1029/92JB02272.
Houliston, D. J., G. Waugh, and J. Laughlin (1984), Automatic real-time event detection for seismic networks, *Comput. Geosci.*, *10*(4), 431–436, doi:10.1016/0098-3004(84)90043-8.
Kastens, K. A., W. B. F. Ryan, and P. J. Fox (1986), Structural and volcanic expression of a fast slipping ridge-transform-ridge-plate boundary: Sea MARC I and photographic surveys at the Clipperton transform fault, *J. Geophys. Res.*, *91*(B3), 3469–3488, doi:10.1029/JB091iB03p03469.
Knuepfer, P. L. K. (1989), Implications of the characteristics of end-points of historical surface fault ruptures for the nature of fault segmentation, *U.S. Geol. Surv. Open-File Rep.*, *89–315*, 193–228.
Kreemer, C., W. E. E. Holt, and A. J. Haines (2003), An integrated global model of present-day plate motions and plate boundary deformation, *Geophys. J. Int.*, *154*(1), 8–34, doi:10.1046/j.1365-246X.2003.01917.x.
Liu, Y., J. J. McGuire, and M. D. Behn (2012), Frictional behavior of oceanic transform faults and its influence on earthquake characteristics, *J. Geophys. Res.*, *117*, B04315, doi:10.1029/2011JB009025.
Lonsdale, P. (1978), Near-bottom reconnaissance of a fast-slipping transform fault zone at the Pacific-Nazca plate boundary, *J. Geol.*, *86*, 451–472.
Lonsdale, P. (1994), Structural geomorphology of the Eltanin fault system and adjacent transform faults of the Pacific-Antarctic plate boundary, *Mar. Geophys. Res.*, *16*(2), 105–143.
McGuire, J. J. (2008), Seismic cycles and earthquake predictability on East Pacific Rise transform faults, *Bull. Seismol. Soc. Am.*, *98*(3), 1067–1084.
McGuire, J. J., and J. A. Collins (2013), Millimeter-level precision in a seafloor geodesy experiment at the Discovery transform fault, East Pacific Rise, *Geochem. Geophys. Geosyst.*, *14*, 4392–4402, doi:10.1002/ggge.20225.
McGuire, J. J., J. A. Collins, P. Gouédard, E. C. Roland, D. Lizarralde, M. S. Boettcher, M. D. Behn, and R. D. van der Hilst (2012), Variations in earthquake rupture properties along the Gofar transform fault, East Pacific Rise, *Nat. Geosci.*, *5*(5), 336–341, doi:10.1038/ngeo1454.
Naar, D. F., and R. N. Hey (1991), Tectonic evolution of the Easter microplate, *J. Geophys. Res.*, *96*(B5), 7961–7993, doi:10.1029/90JB02398.
Nishimura, C. E., and D. W. Forsyth (1988), Rayleigh wave phase velocities in the Pacific with implications for azimuthal anisotropy and lateral heterogeneities, *Geophys. J. Int.*, *94*, 479–501, doi:10.1111/j.1365-246X.1988.tb02270.x.
Phipps Morgan, J., and D. W. Forsyth (1988), Three-dimensional flow and temperature perturbations due to a transform offset: Effects on oceanic crustal and upper mantle structure, *J. Geophys. Res.*, *93*(B4), 2955–2966, doi:10.1029/JB093iB04p02955.
Pickle, R. C., D. W. Forsyth, N. Harmon, A. N. Nagle, and A. Saal (2009), Thermo-mechanical control of axial topography of intra-transform spreading centers, *Earth Planet. Sci. Lett.*, *284*(3-4), 343–351.
Roland, E. C., D. Lizarralde, J. J. McGuire, and J. A. Collins (2012), Seismic velocity constraints on the material properties that control earthquake behavior at the Quebrada-Discovery-Gofar transform faults, East Pacific Rise, *J. Geophys. Res.*, *117*, B11102, doi:10.1029/2012JB009422.
Searle, R. C. (1983), Multiple, closely spaced transform faults in fast-slipping fracture zones, *Geology*, *11*(10), 607–610.
Shah, A. K., and W. R. Buck (2001), Causes for axial high topography at mid-ocean ridges and the role of crustal thermal structure, *J. Geophys. Res.*, *106*(12), 30,865–30,879, doi:10.1029/2000JB000079.
Sibson, R. H. (1987), Earthquake rupturing as a mineralizing agent in hydrothermal systems, *Geology*, *15*(8), 701–704.
Simons, F. J., B. D. E. Dando, and R. M. Allen (2006), Automatic detection and rapid determination of earthquake magnitude by wavelet multiscale analysis of the primary arrival, *Earth Planet. Sci. Lett.*, *250*(1-2), 214–223, doi:10.1016/j.epsl.2006.07.039.
Small, C. (1998), Global systematics of mid-ocean ridge morphology, in *Faulting and Magmatism at Mid-Ocean Ridges*, edited by W. Roger Buck et al., AGU, Washington, D. C., doi:10.1029/GM106p0001.
Smith, D. K. (2003), Spatial and temporal distribution of seismicity along the northern Mid-Atlantic Ridge (15°−35°N), *J. Geophys. Res.*, *108*(B3), 2167, doi:10.1029/2002JB001964.
Sverdrup, K. A. (1987), Multiple-event relocation of earthquakes near the Gorda Rise: Mendocino fracture zone intersection, *Geophys. Res. Lett.*, *14*(4), 347–350, doi:10.1029/GL014i004p00347.
Sykes, L. R., and G. Ekström (2012), Earthquakes along Eltanin transform system, SE Pacific Ocean: Fault segments characterized by strong and poor seismic coupling and implications for long-term earthquake prediction, *Geophys. J. Int.*, *188*(2), 421–434, doi:10.1111/j.1365-246X.2011.05284.x.
Valoroso, L., L. Chiaraluce, and C. Collettini (2014), Earthquakes and fault zone structure, *Geology*, *42*(4), 343–346, doi:10.1130/G35071.1.
Waldhauser, F., and W. L. Ellsworth (2000), A double-difference earthquake location algorithm: Method and application to the northern Hayward fault, California, *Bull. Seismol. Soc. Am.*, *90*(6), 1353–1368.
Wesnousky, S. G. (2006), Predicting the endpoints of earthquake ruptures, *Nature*, *444*(7117), 358–360.